

AKÜ FEMÜBİD 22 (2022) 025701 (342-352)

AKU J. Sci. Eng. 22 (2022) 025701 (342-352)

DOI: 10.35414/akufemubid.1018774

Araştırma Makalesi / Research Article

# Application of Classical Lamination Theory to Fused Deposition Method 3-D Printed Plastics and Full Field Surface Strain Mapping

Cagatay YILMAZ<sup>1\*</sup>, Hafiz Qasim ALI<sup>2</sup>, Mehmet YILDIZ<sup>3</sup><sup>1</sup>Abdullah Gül University, Faculty of Engineering, Mechanical Engineering, Kayseri.<sup>2</sup>Sabancı University, Faculty of Engineering and Natural Sciences, Istanbul<sup>3</sup>Sabancı University, Faculty of Engineering and Natural SciencesCorresponding author\* e-posta<sup>1</sup>: yilmaz.cagatay@agu.eduORCID ID: <https://orcid.org/0000-0002-8063-151X>e-posta<sup>2</sup>: hafizqasimali@sabanciuniv.eduORCID ID: <https://orcid.org/0000-0001-8288-2737>e-posta<sup>3</sup>: mehmet.yildiz@sabanciuniv.eduORCID ID: <https://orcid.org/0000-0003-1626-5858>

Geliş Tarihi: 03.11.2021

Kabul Tarihi: 22.03.2022

## Abstract

In this study, five differently oriented sets of 3D-printed tensile samples are produced using the Fused Deposition Method (FDM). Among these five sets, three are used to determine the elastic constant to be used in Classical Lamination Theory (CLT), which is generally used to model fiber-reinforced polymers (FRP). Based on the obtained results, CLT is further applied to the remaining two sets of unreinforced 3D-printed polymer samples where the deposition direction varies in each layer. The stress and strain calculated with CLT are then compared with experimental results obtained through tensile testing. The comparison depicts that experimental and CLT results are in good agreement at lower strain levels. In contrast, the stress calculated with CLT deviates from the experimental result at the higher strain levels. Thereafter, a full-field surface strain mapping is applied by using Digital Image Correlation (DIC) Techniques to reveal the damage progression and failure of Fused Deposition Method 3-D Printed Plastics.

## Keywords

3D Plastic Printer;  
Fused Deposition  
Method; Classical  
Lamination Theory;  
Polymer; Tensile Test;  
DIC

# Klasik Laminasyon Teorisinin Üç Boyutlu Yazıcı ile Eriyik Yığma Modelleme Yöntemi Kullanılarak Üretilmiş Plastiklere Uygulanması ve Tam Alanlı Yüzey Gerinim Haritalanması

## Öz

Bu çalışmada üç boyutlu yazıcı ile Eriyik Yığma Modelleme (EYM) yöntemi kullanılarak farklı yazma yönlerindeki katmanlara sahip toplamda beş set çekme örneği üretilmiştir. Üretilen üç farklı sete çekme testi yapılarak farklı yönlerdeki elastik sabitler daha sonra Klasik Laminasyon Teorisinde (KLT) kullanılmak üzere ölçülmüştür. Klasik Laminasyon Teorisi genel olarak tek yönlü fiberler ihtiva eden polimerik yapıların modellenmesi için kullanılmaktadır. Bu çalışma ile KLT üç boyutlu yazıcı ile üretilen ve içerisinde herhangi bir fiber takviyesi ihtiva etmeyen ve her katmanda yazma yönleri değişen iki farklı polimerik yapıya uygulanmıştır. KLT ile elde edilen gerinim ve gerilme değerleri çekme deneyi ile elde edilen gerinim ve gerilme değerleri ile karşılaştırılmıştır. Elde edilen sonuçlara göre düşük gerinim değerleri için KLT ile elde edilen sonuçların deneysel sonuçlar ile uyumlu olduğu, yalnız gerinim değeri arttıkça KLT ile hesaplanan değerlerinin deneysel değerlerden uzaklaştığı görülmüştür. Daha sonra ise Eriyik Yığma Modelleme Yöntemi ile üretilen üç boyutlu plastiklerin hasar ilerlemesi ve kırılması Dijital Görüntü Korelasyon Tekniği ile Tam Alanlı Yüzey Gerinim Haritalanması kullanılarak çıkarılmıştır.

## Anahtar kelimeler

Üç Boyutlu Plastik  
Yazıcı; Eriyik Yığma  
Modelleme; Klasik  
Katmanlama Teorisi;  
Polimer; Çekme Testi;  
Dijital Görüntü  
Korelasyon

## 1. Introduction

Recent advancements in manufacturing and the design of complex structures signify the importance of 3D printing technology due to its capability for rapid prototyping, reverse engineering, and manufacturing a part in limited quantities without any molding requirement. These capabilities render 3D printing technology appealing for industries such as automotive (Erşan *et al.* 2018, Yavuz *et al.* 2021), medical application (Love *et al.* 2014), aerospace (Joshi and Sheikh 2015), robotics (Sachyani Keneth *et al.* 2021), and construction (Tay *et al.* 2017). 3D printing technology uses materials such as thermoplastic polymers, cement, metal, cell, and tissue to shape the final body (Lee *et al.* 2017). Techniques used in 3D printing are direct ink writing (DIW), selective laser sintering (SLS), electron beam melting (EBM), stereolithography (SLA), and fused deposition method (FDM) (Karakurt and Lin 2020). Among these techniques, the fused deposition method (FDM) is the most widely used due to its simplicity and low cost.

FDM extrudes a thermoplastic polymer filament through a hot nozzle and deposits it in successive layers to form a 3D printed part. There are several parameters that can influence the mechanical behaviors of FDM 3D-printed parts. Among these parameters, the most significant ones are nozzle temperature, bed temperature, printing speed, flow rate, infill pattern type, fill rates, and deposition direction. The effect of nozzle temperature (Bacak *et al.* 2020), bed temperature (Kumar *et al.* 2018), fill rates (Kamaal *et al.* 2021), infill pattern type (Demircioğlu *et al.* 2018) are studied. Although these parameters have a particular effect on the mechanical properties of FDM 3D-printed parts, once these parameters are optimized, the most significant remaining variable is the direction of the deposition. The direction of deposition for the FDM process attracts many authors' attention (Alexander *et al.* 1998, Ghorpade *et al.* 2007, S H Masood *et al.* 2003, Syed H Masood *et al.* 2000, Pandey *et al.* 2004, Thrimurthulu *et al.* 2004). The deposition direction is studied to minimize the volume of material used in 3D printing (Syed H Masood *et al.* 2000).

Recent studies focus on optimizing the deposition parameters and appropriate printing direction for an FDM 3D printing process so that cost and time-effective parameters can be utilized for the printing. The deposition direction is analyzed to predict the least required printing time and the lowest cost (Alexander *et al.* 1998). A generic and multicriteria genetic algorithm is developed to find the optimized direction of deposition based on the volumetric error between final body volume and calculated volume prior to printing (Kiendl and Gao 2020, Kumar *et al.* 2018).

In addition to these studies, numerous experimental studies in the literature consider the direction of printing on the mechanical properties of FDM 3D-printed parts (Giri *et al.* 2021, Hanon *et al.* 2020, Kiendl and Gao 2020, Popescu *et al.* 2018, Zaldivar *et al.* 2017). In addition to experimental studies, some theoretical studies can be found in the literature. In one study, the elastic modulus of short carbon fiber (SCF) reinforced polycarbonate FDM 3D-part is predicted with CLT, and it is shown that as the volume fraction of SCF increases, predicted values converge to experimental ones (Gupta *et al.* 2020). Using a combination of CLT and Tsai-Hill failure theory, the stiffness and strength at macro-scale can be predicted for Acrylonitrile Butadiene Styrene (ABS) polymer 3D-printed parts (Alaimo *et al.* 2017).

However, further investigation on the predictability of stress with respect to an applied strain of FDM 3D-printed parts, with commonly used polymer, polylactic acid (PLA), is required along with the damage initiation and progression by using a Digital Image Correlation Technique.

Herein, we present a combined experimental and numerical study to investigate the predictability of strain to applied stress for FDM 3D-printed parts with layer-wise variable directional deposition by using the polymer PLA. In order to predict the mechanical response, Classical Lamination Theory (CLT), which is already applicable to laminated composites structures, is applied to FDM 3D-printed parts. The attained stress and strain values are compared with experimental data acquired from digital image correlation (DIC) under tensile loading. Finally, a full-field surface strain map is used to

understand the damage initiation, progression, and failure of a 3D-printed polylactic acid (PLA) polymer part produced by changing the deposition direction.

**2. Material and Method**

**2.1 Materials and sample preparation**

The mechanical tensile test samples are manufactured from a single PLA (polylactic acid) filament spool with a Fused Deposition Method 3D-printer (Raise 3D Pro2 Plus). The filament used in this study has a diameter of 1.75 mm, and it is extruded from a circular nozzle with a diameter of 0.4 mm. The 3D printer has 0.78125 and 0.078125  $\mu\text{m}$  positioning resolution on the X/Y axis and Z axis, respectively.

The layer height of 0.2 mm, bed temperature of 80  $^{\circ}\text{C}$ , and nozzle temperature of 210  $^{\circ}\text{C}$  are chosen as process parameters. Before the 3D printing of each sample, a 1.82 mm raft platform is produced to create an interface between the heated bed and specimens. This interface prevents the passage of scratches on the heated bed onto the sample, enabling the production of test samples with high surface quality.

In this study, the direction parallel to the length of the specimen and the direction along the width of the specimen is referred to as direction 0 $^{\circ}$  and 90 $^{\circ}$ , respectively. +45 $^{\circ}$  and -45 $^{\circ}$  are taken in the counterclockwise and clockwise directions, respectively, with respect to the 0 $^{\circ}$  direction, as shown in Figure 1. All specimen is loaded in the lengthwise direction as depicted in Figure 1.

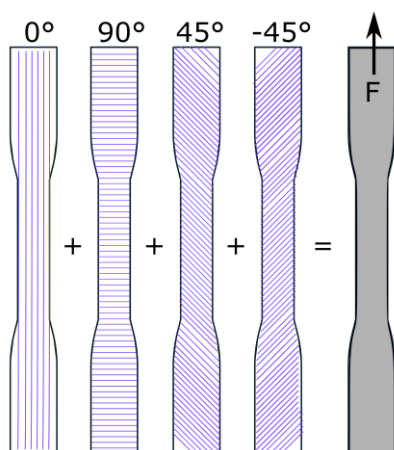


**Figure 1.** The direction of deposition and loading

Overall, five different batches of specimens are produced, and all the specimens used in this study consist of fifteen layers of PLA filament. The batch I and Batch II specimens are produced by depositing extruded filament on the 0 $^{\circ}$  and 90 $^{\circ}$ , respectively. Batch III specimens are produced with the alternating deposition directions, as +45 $^{\circ}$  and -45 $^{\circ}$ , in every layer with respect to the 0 $^{\circ}$ . Batch IV is produced by alternating the deposition direction as 90 $^{\circ}$  and 0 $^{\circ}$  for every layer. Batch V is produced alternating the direction of deposition as 90 $^{\circ}$ , 60 $^{\circ}$ , 30 $^{\circ}$ , and 0 $^{\circ}$  for every layer. In Table 1, the direction of deposition for each layer can be seen.

Dimensions of specimens are chosen based on the ASTM D 638-14 standard type I specimen (Internasional 2014).

**Table 1.** Batch number and the direction of deposition to the applied load.

No	Direction of deposition
I	[0] <sub>15</sub>
II	[90] <sub>15</sub>
III	[+45/-45/+45/-45/+45/-45/+45/-45/+45/-45/+45/-45/+45]
IV	[90/0/90/0/90/0/90/0/90/0/90/0/90/0/90]
V	[90/60/30/0/90/60/30/0/90/60/30/0/90/60/30]

**2.2 Mechanical testing**

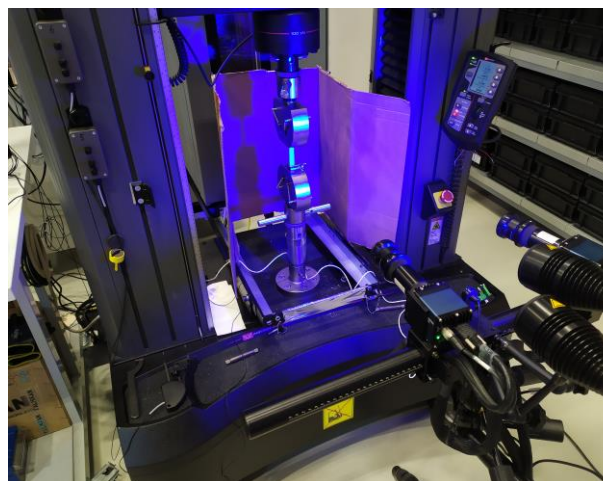
All tensile tests are performed with an Instron 8801 electromechanical Universal Test Machine (UTM) equipped with a load cell of  $\pm 100\text{kN}$ . Once samples are attached to UTM, a preload of 5 N is applied to compensate for backlash. The control of the UTM machine and data acquisition, such as strains (axial and transverse) and load, are done with Bluehill 3 software. Instron 2630-112 axial extensometer with a gauge length of 50 mm and Epsilon 3542 transverse extensometer with a gauge length of 13 mm are used to measure the strain in the direction of load and direction perpendicular to load, respectively. A crosshead displacement of 5 mm/min is chosen as recommended by the ASTM D 638-14 standard for the tensile test. Furthermore, shear tests are performed as per the direction of the ASTM D3518 standard.

### 2.3 Digital Image Correlation (DIC)

Digital image correlation is an optical-based non-contact and full-field measurement technique implicated in measuring the strain distribution over the surface of the specimen. With the assistance of black (RAL code 9005) and white (RAL code 9010) paints, a speckle pattern was created on the surface of the gauge length of the specimen. Two broken tensile test samples with a speckle pattern from Batch IV can be seen in Figure 2 (a). The 2D-DIC analysis is conducted with the help GOM (Braunschweig-Germany) 12M sensor system calibrated as per the manufacturer’s instruction based on the measuring volume of 100 x 75mm via CP20-90 x 72 calibration object. During the experimental measurements made with the DIC method, 635 mm working distance and 25° camera angle were set for the single-shot mode for the calibration of the sensor. The obtained calibration results are calibration deviation= 0.022 pixels (limit value: 0.050 pixels) and scale deviation= 0.001mm (limit value: 0.0008mm). While performing the mechanical test, a facet size of 25 and a step size of 19 pixels are chosen to track the displacement. Furthermore, the pattern quality is inspected with the help of ARAMIS professional software, and the visual extensometers of 5mm (Figure 3) in both X and Y directions were applied on the surface of the Batch III specimens to calculate the shear strain, which is necessary to compute the shear modulus ( $G_{12}$ ).



(a)



(b)

**Figure 2.** a) Tensile test samples with spackle pattern for DIC, b) Tensile test setup with DIC cameras

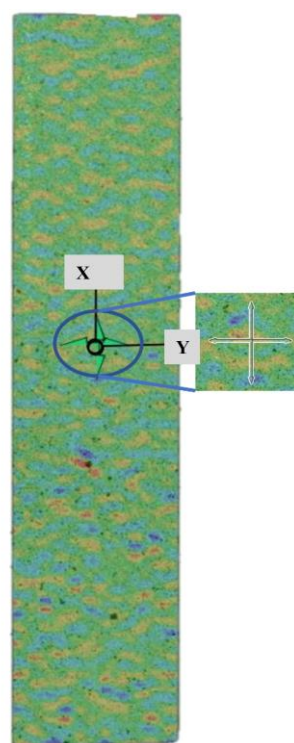


**Figure 3.** Representative DIC specimen

## 3. Results and Discussion

### 3.1 Classical Lamination Theory

Quasi-static tensile and in-plane shear tests are performed to measure elastic constants and their dependency on the deposition direction of the FDM 3D-printed plastic. Four different elastic constants, in-plane shear modulus ( $G_{12}$ ), longitudinal elastic modulus ( $E_{11}$ ), transverse elastic modulus ( $E_{22}$ ), and major Poisson’s ratio ( $\nu_{12}$ ), are measured based on the above-mentioned mechanical tests and minor Poisson’s ratio ( $\nu_{21}$ ) is calculated by using Equation (1), and obtained results are tabulated in

Table 2.

$$v_{21} = \frac{v_{12}}{E_{11}} * E_{22} \tag{1}$$

Although a molded plastic shows isotropic behavior, in

Table 2, FDM 3D printed plastic indicates directional properties. When the deposition direction is parallel to the applied load, the measured elastic constant  $E_{11}$  is 2.82 GPa while transverse elastic modulus  $E_{22}$  is 1.58 GPa.

**Table 2.** Engineering constants of FDM 3D-printed plastic

Engineering Constants	Mean	COV
$E_{11}$	2.82 GPa	1.89 %
$G_{12}$	0.59 GPa	6.9 %
$E_{22}$	1.58 GPa	3.05 %
$v_{12}$	0.36	2.06 %
$v_{21}$	0.20	

Classical lamination theory (CLT) with a transversely isotropic symmetry is applied to FDM 3D-printed plastic to predict stress valued for respected strain values on the top surface of the first layer. After that, values calculated by CLT are compared with the values measured during the tensile test in the elastic region of the stress-strain curve. CLT considers plane stress assumption, and if a load or strain is known at any point of any layer along with the thickness, global stress and strain can be calculated for any layer according to Equation (2).

$$\begin{bmatrix} \sigma_x \\ \sigma_y \\ \tau_{xy} \end{bmatrix} = \begin{bmatrix} \bar{Q}_{11} & \bar{Q}_{12} & \bar{Q}_{16} \\ \bar{Q}_{12} & \bar{Q}_{22} & \bar{Q}_{26} \\ \bar{Q}_{16} & \bar{Q}_{26} & \bar{Q}_{66} \end{bmatrix} \begin{bmatrix} \varepsilon_x \\ \varepsilon_y \\ \gamma_{xy} \end{bmatrix} \tag{2}$$

Here is  $\sigma_x, \sigma_y, \tau_{xy}$  are the stress components along the x-direction, y-direction, and xy-plane, respectively. In CLT, x-direction and y-direction refer to global axes, whereas directions 1, 2, and 3 refer to material axes. For simplicity, x-direction refers to the direction parallel to the length of the specimen (0° direction), and y-direction is along the width of the specimen (90° direction), which can also be seen in Figure 3.  $\bar{Q}_{ij}$  is the reduced transformed stiffness

matrix, and a detailed calculation can be found in Panbarasu et al. 2021.

Strain at any point on any layer can be expressed by mid-plane strains ( $\varepsilon_x^0, \varepsilon_y^0, \gamma_{xy}^0$ ), curvature ( $\kappa_x, \kappa_y, \kappa_{xy}$ ), and location of the layer through the thickness (z) as given in Equation (3).

$$\begin{bmatrix} \varepsilon_x \\ \varepsilon_y \\ \gamma_{xy} \end{bmatrix} = \begin{bmatrix} \varepsilon_x^0 \\ \varepsilon_y^0 \\ \gamma_{xy}^0 \end{bmatrix} + z \begin{bmatrix} \kappa_x \\ \kappa_y \\ \kappa_{xy} \end{bmatrix} \tag{3}$$

Generally, stress components in Equation (2) can be expressed in terms of forces per unit width and moments. And the relation between forces per unit width, moments, midplane strains and curvature can be written in terms of Equation (4)

$$\begin{bmatrix} N_x \\ N_y \\ N_{xy} \\ M_x \\ M_y \\ M_{xy} \end{bmatrix} = \begin{bmatrix} A_{11} & A_{12} & A_{16} & B_{11} & B_{12} & B_{16} \\ A_{12} & A_{22} & A_{26} & B_{12} & B_{22} & B_{26} \\ A_{16} & A_{26} & A_{66} & B_{16} & B_{26} & B_{66} \\ B_{11} & B_{12} & B_{16} & D_{11} & D_{12} & D_{16} \\ B_{12} & B_{22} & B_{26} & D_{12} & D_{22} & D_{26} \\ B_{16} & B_{26} & B_{66} & D_{16} & D_{26} & D_{66} \end{bmatrix} \begin{bmatrix} \varepsilon_x^0 \\ \varepsilon_y^0 \\ \gamma_{xy}^0 \\ \kappa_x \\ \kappa_y \\ \kappa_{xy} \end{bmatrix} \tag{4}$$

Here [A] is the extensional stiffness matrix, [B] is the coupling stiffness matrix, and [D] is the bending stiffness matrix and can be calculated by Equations (5), (6), and (7), respectively.

$$A_{ij} = \sum_{k=1}^n [(\bar{Q}_{ij})]_k (h_k - h_{k-1}), \tag{5}$$

$$i=1,2,6; j=1,2,6$$

$$B_{ij} = \frac{1}{2} \sum_{k=1}^n [(\bar{Q}_{ij})]_k (h_k^2 - h_{k-1}^2), \tag{6}$$

$$i=1,2,6; j=1,2,6$$

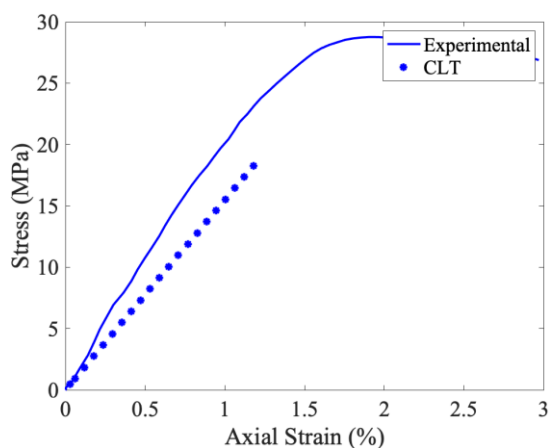
$$D_{ij} = \frac{1}{3} \sum_{k=1}^n [(\bar{Q}_{ij})]_k (h_k^3 - h_{k-1}^3), \tag{7}$$

$$i=1,2,6; j=1,2,6$$

Six different equations are derived from equation (4) for a known load per unit width, and simultaneous solution of these six different equations results in midplane strains and curvatures. Once the midplane strains and curvatures are calculated, strains can be calculated on any layer.

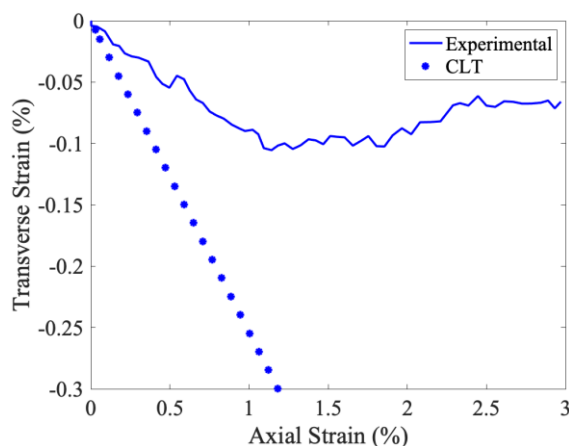
Figure 4 illustrates an experimental and CLT-based comparison of axial stress and strain values for Batch IV. However, the stress values at the lower strain level for CLT and experiment agree, as the

strain increases, stress values calculated with CLT deviate from experimental stress values.



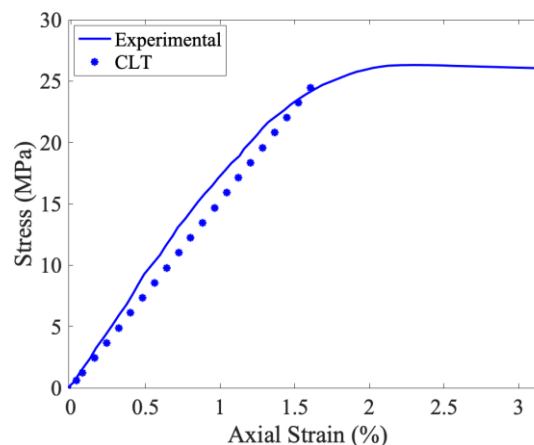
**Figure 4.** Comparison of experimental and CLT results for Batch IV

Figure 5 shows a significant difference between the transverse strain values measured by DIC and calculated by CLT for Batch IV. This significant difference between the DIC measured values, and CLT calculated values can be explained by the occurrence of micro-cracks during the experiment. First, CLT assumes an elastic deformation without considering any damage formation. However, in experiments, transverse cracks can be formed between the deposited filaments in  $90^\circ$  direction and inhibit the load transfer between the deposited layers and filaments. As the load increases, there is a surge in micro-cracks formation, which prevents the load transfer from the axial direction to the transverse direction. Consequently, experimentally measured transverse strain with respect to applied axial strain starts to deviate from theoretical transverse strain calculated by CLT due to an increase in the transverse crack density. Even after some point ( $\sim 1.2\%$  axial strain), transverse cracks are saturated, and experimentally measured transverse strain does not change significantly, whereas CLT-calculated transverse strain shows a linear trend. This phenomenon is also reported in the literature for FRP, which has glass fibers in  $90^\circ$  direction (Yilmaz et al. 2016).



**Figure 5.** Comparison of experimental and CLT results for batch IV

The evolution of axial strain to applied axial stress can be seen in Figure 6 for batch V, and it can be observed that the prediction of axial stress is better than the case of batch IV.



**Figure 6.** Comparison of experimental and CLT results for Batch V

Figure 7 reveals the CLT-predicted and experimentally measured transverse strain to axial strain for batch V. It depicts a relatively better correlation between the CLT and experiments for batch V compared to batch IV for transverse strain. This relatively better correlation for transverse strain might be due to the reduced number of  $90^\circ$  filaments layer for Batch V. Batch V has only four layers of  $90^\circ$  filaments, whereas batch IV has eight layers of  $90^\circ$  filaments.  $90^\circ$  filament layers are responsible for transverse crack formation. A decrease in the number of  $90^\circ$  filament layers causes a reduction in the number of transverse cracks. Thus, the load transfer from the axial

direction to the lateral direction is not interrupted. As the axial load increases, transversal load also increases. So the increase in the transversal load causes more contraction in the lateral direction.

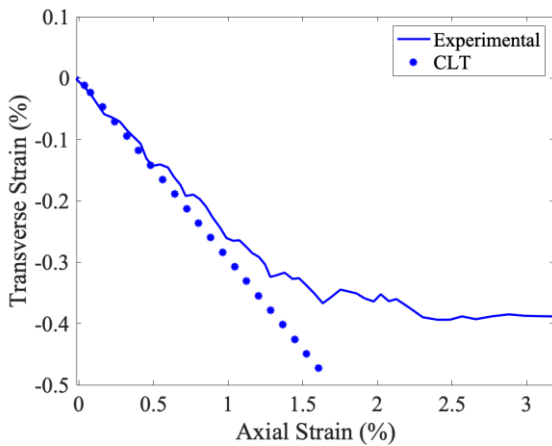


**Figure 7.** Comparison of experimental and CLT results for batch V

### 3.2. Digital Image Correlation

The full-field strain contours of the specimens are obtained through ARAMIS professional 2016 software, where “3-2-1 alignment” is used to define the coordinate system for synchronizing the DIC alignment as per the Instron loading direction. Figure 8, Figure 9, and Figure 10 represent the specimens’ strain ( $\epsilon_x$ ) contours at different percentages of the load. In the case of Batch III specimen (Figure 8), the strain is distributed across the specimen, indicating that load from Instron is appropriately distributed across the gauge length of the specimen, which will not be the case if there are defects or a high-stress concentration region inside the specimen. As the load progresses at 50%, the higher strain is located at the top and bottom region of the specimen due to the grips, while the middle region of the gauge length has lower strain distribution. As the load progresses towards 70% to 100%, the shear imprints start arising predominantly due to the 45° deposition direction, which causes in-plane shear strength inside the specimen.

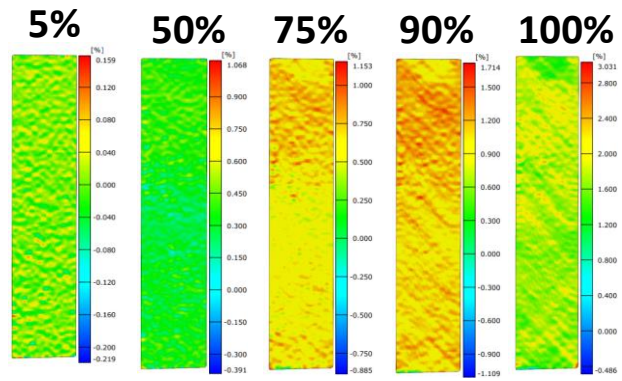


**Figure 8.** A strain map evolution of a representative specimen from batch III

In the case of the Batch IV specimen (Figure 9), the strain concentration is higher at the top of the gauge length, which is closer to the moving head of the Instron. At 50% load level, the strain is distributed across the specimen, but the higher concentration is near the top and bottom grip. It can be observed that at 75% load level, the strain field is divided into high and low strain regions inside the gauge length due to 0° and 90° deposition direction. The 90° deposition is in the transverse direction to the loading direction, which causes failure initiation at a lower load level visible in 75% load level contour. It progresses up to 100% load level, and this transverse crack propagation causes failure of the specimen.

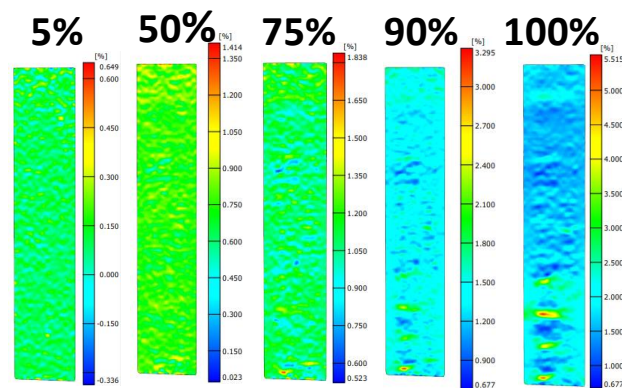


**Figure 9.** A strain map evolution of a representative specimen from batch IV

Figure 10 represents the Batch V specimen where at lower load level (5%), the strain distribution is heterogeneous, and even at lower load level, higher strain is recorded at the top grip of the specimen. At 50% load level, the shear imprint is significant near the top grip region while the bottom grip region

shows lower strain region formation, which depicts that the load is heterogeneously distributed across the gauge length. At 100% load level, the shear imprints are predominantly visible near the upper part of the gauge length, while the bottom part of the gauge length has a lower strain.

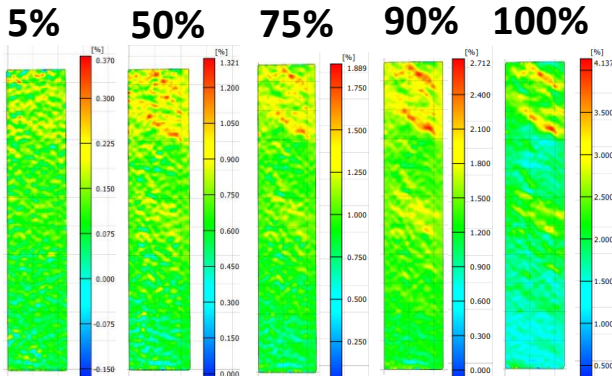


**Figure 10.** A strain map evolution of a representative specimen from batch V

After reaching the ultimate tensile load, the load starts decreasing, and the plastic specimens where plastic deformation has initiated progress, which decreases the load. In Figure 11 (a), four different points are marked for a Batch III specimen, and their correspondent strain contours are also exhibited at In Figure 11 (b). At “point 1,” where load starts declining, the shear imprints can be observed, whereas at “point 2,” the global failure initiated near the bottom grip. It progresses in a 45° direction, which is visible in the “point 3” strain map and causes final failure at “point 4”.

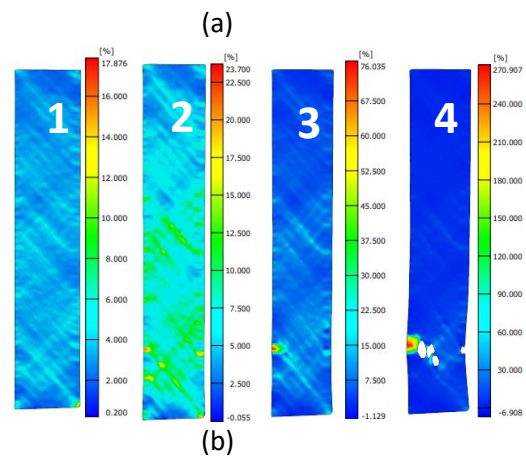
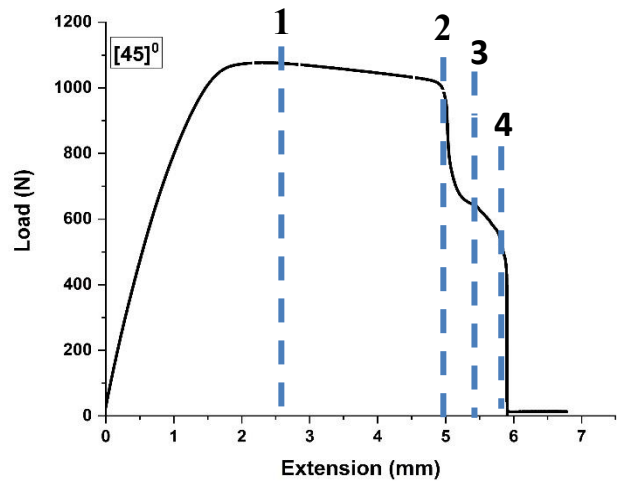


**Figure 11.** (a) Load-extension graph, and (b) Strain evolution of a Batch III specimen

Similarly, in Batch IV specimen, Figure 12 (a) and (b) exhibits the load vs. extension curve, and two points are marked on this curve along with their corresponding strain distribution images. At “point 1” highlights the formation of a major crack which initiated due to accumulation at the earlier stages of the test as already shown in Figure 8. This major crack further progresses and causes global failure, indicated by “point 2”.

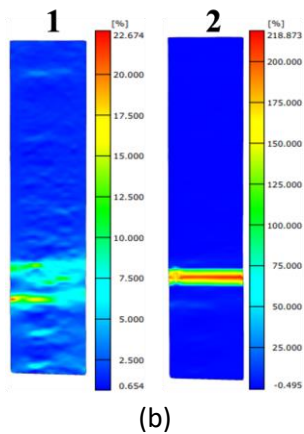
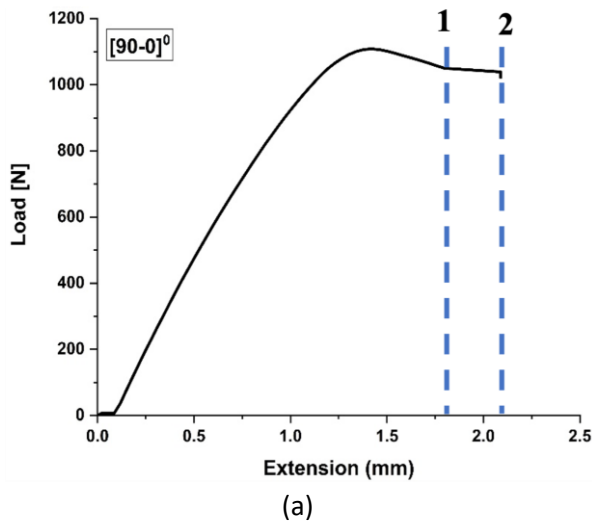


**Figure 12.** (a) Load-extension graph, and (b) Strain evolution of a Batch IV specimen

In the case of Batch V, the heterogeneous strain distribution across the gauge length until ultimate tensile load (Figure 10) causes failure initiation, which causes the decrease in load and plastic deformation inside the specimen. During the plastic deformation region, two points are highlighted in Figure 13 (a) and their strain evolution can be seen in Figure 13 (b). The “point 1” initiates immediately after the ultimate tensile strength, where high strain imprints are visible near the top grip and middle section of the gauge length. As the test proceeds, the specimen fails at “point 2,” and the failure occurs near the top grip. From the strain contours of the fused deposited 3D printed plastic specimens, it can be stated that DIC can predict the failure region even at lower load levels.

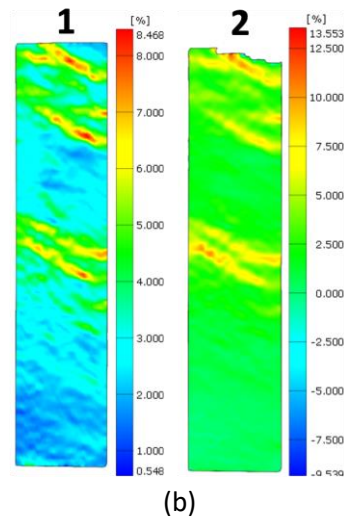
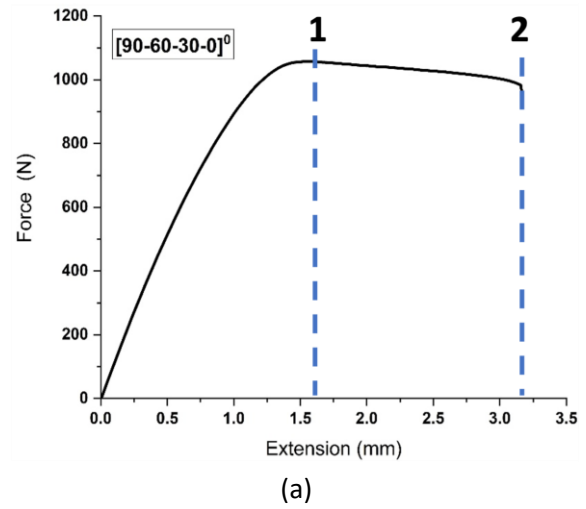


**Figure 13.** (a) Load-extension graph, and (b) Strain evolution of a Batch V specimen.

#### 4. Conclusion

This study aims to analyze the applicability of CLT theory to FDM 3D printed plastic parts by analyzing damage initiation and progression by using Digital Image Correlation techniques. For that purpose, plastic tensile test samples are produced with different deposition angles. Elastic constants, such as in-plane shear modulus ( $G_{12}$ ), longitudinal elastic modulus ( $E_{11}$ ), transverse elastic modulus ( $E_{22}$ ), and major Poisson’s ratio ( $\nu_{12}$ ), are calculated experimentally, then used for the Classical Lamination Theory for two different sets of samples. The strain field on the surface of the batch IV & V samples is measured with a DIC camera to compare it with CLT-calculated axial and transversal strains. After that, full-field surface strain mapping of corresponding batches reveals the failure of FDM 3D-printed samples with alternating deposition

directions in each layer under the tensile load. Following conclusions are drawn in this study:

- 1) It can be observed that the direction of deposition significantly affects the elastic properties of FDM 3D printed samples.
- 2) Axial stress and strain values calculated by Classical Lamination Theory, which considers a transversely isotropic material symmetry, can be validated by experimentally measured values.
- 3) Transverse strain measured by the DIC camera indicates a different trend than that calculated with CLT for batch IV. It can be concluded that this significant difference between the experiment and CLT comes from the transverse crack. In the experiment, load transfer from the axial direction to the transverse direction is interrupted as the density of transverse crack increases. Thus, axial stress is not transferred to the transverse direction. As a result, the tensile test sample does not experience a contraction as much as predicted by CLT.
- 4) For both batch IV & V, when compared with the experiment, CLT underestimates the stress values corresponding to the same axial strain. Although a clear explanation for this behavior is not found, this behavior is also reported in the literature for FDM 3D printed tensile samples. (Casavola *et al.* 2016).
- 5) With the DIC, It is possible to reveal shear imprints over the surface of 3D-printed polymers as well as damage initiation and progression with a final failure.

#### **Acknowledgment**

This work was partially supported by the Faculty of Engineering at Abdullah Gul University (AGU) and Sabancı University Integrated Manufacturing Research (SU-IMC) and Application Center. The authors gratefully acknowledge the help of Aynur Akgül (AGU) for production of FDM 3D-printed samples and Umut Kılıç (SU-IMC) for his help in mechanical testing.

#### **5. References**

Alaimo, G., Marconi, S., Costato, L., & Auricchio, F. 2017. Influence of meso-structure and chemical

composition on FDM 3D-printed parts. *Composites Part B: Engineering*, **113**, 371–380.

Alexander, P., Allen, S., & Dutta, D. 1998. Part orientation and build cost determination in layered manufacturing. *Computer-Aided Design*, **30(5)**, 343–356.

Bacak, S., Varol, H. V. Ö., & Tatlı, M. 2020. Fdm Yöntemi İle Üretilen Pla Numunelerin Çekme Özelliklerine İşlem Parametrelerinin Etkisinin İncelenmesi. *Mühendislik Bilimleri ve Tasarım Dergisi*, **9(1)**, 209–216.

Casavola, C., Cazzato, A., Moramarco, V., & Pappalettere, C. 2016. Orthotropic mechanical properties of fused deposition modelling parts described by classical laminate theory. *Materials & Design*, **90**, 453–458.

Demircioğlu, P., Sucuoğlu, H. S., Böğrekci, İ., & Gültekin, A. 2018. The effect of three dimensional printed infill pattern on structural strength. *El-Cezeri Journal of Science and Engineering*, **5(3)**, 785–796.

Erşan, K., Demiroğlu, Y. A., & Güldür, B. 2018. Design and Manufacturing of Real-Scale-Mockup-Car Door Via 3d Printer. *Journal of New Results in Science*, **7(3)**, 54–66.

Ghorpade, A., Karunakaran, K. P., & Tiwari, M. K. 2007. Selection of optimal part orientation in fused deposition modelling using swarm intelligence. *Proceedings of the Institution of Mechanical Engineers, Part B: Journal of Engineering Manufacture*, **221(7)**, 1209–1219.

Giri, J., Chiwande, A., Gupta, Y., Mahatme, C., & Giri, P. 2021. Effect of process parameters on mechanical properties of 3d printed samples using FDM process. *Materials Today: Proceedings*, **47**, 5856–5861.

Gupta, A., Fidan, I., Hasanov, S., & Nasirov, A. 2020. Processing, mechanical characterization, and micrography of 3D-printed short carbon fiber reinforced polycarbonate polymer matrix composite material. *The International Journal of Advanced Manufacturing Technology*, **107(7)**, 3185–3205.

Hanon, M. M., Alshammas, Y., & Zsidai, L. 2020. Effect of print orientation and bronze existence on tribological and mechanical properties of 3D-printed bronze/PLA composite. *The International Journal of Advanced Manufacturing Technology*, **108(1)**, 553–570.

Internasional, A. 2014. ASTM D638-14 Standard Test Methods for Tensile Properties of Plastic. *America Society for Testing and Material*.

Joshi, S. C., & Sheikh, A. A. 2015. 3D printing in aerospace and its long-term sustainability. *Virtual and Physical*

- Prototyping*, **10(4)**, 175–185.
- Kamaal, M., Anas, M., Rastogi, H., Bhardwaj, N., & Rahaman, A. 2021. Effect of FDM process parameters on mechanical properties of 3D-printed carbon fibre–PLA composite. *Progress in Additive Manufacturing*, **6(1)**, 63–69.
- Karakurt, I., & Lin, L. 2020. 3D printing technologies: techniques, materials, and post-processing. *Current Opinion in Chemical Engineering*, **28**, 134–143.
- Kiendl, J., & Gao, C. 2020. Controlling toughness and strength of FDM 3D-printed PLA components through the raster layup. *Composites Part B: Engineering*, **180**, 107562.
- Kumar, N., Jain, P. K., Tandon, P., & Pandey, P. M. 2018. The effect of process parameters on tensile behavior of 3D printed flexible parts of ethylene vinyl acetate (EVA). *Journal of Manufacturing Processes*, **35**, 317–326.
- Lee, J.-Y., An, J., & Chua, C. K. 2017. Fundamentals and applications of 3D printing for novel materials. *Applied Materials Today*, **7**, 120–133.
- Love, J. D., George, M. J., Aroom, K., & Gill, B. 2014. Inguinal hernia repair using 3 dimensional (3D) printed surgical instruments in the cadaveric model. *Journal of the American College of Surgeons*, **219(4, Supplement)**, e99.
- Masood, S H, Rattanawong, W., & Iovenitti, P. 2003. A generic algorithm for a best part orientation system for complex parts in rapid prototyping. *Journal of Materials Processing Technology*, **139(1)**, 110–116.
- Masood, Syed H, Rattanawong, W., & Iovenitti, P. 2000. Part build orientations based on volumetric error in fused deposition modelling. *The International Journal of Advanced Manufacturing Technology*, **16(3)**, 162–168.
- Panbarasu, K., Ranganath, V. R., & Prakash, R. V. 2021. An investigation on static failure behaviour of CFRP quasi isotropic laminates under in-plane and out-of-plane loads. *Materials Today: Proceedings*, **39**, 1465–1471.
- Pandey, P. M., Thrimurthulu, K., & Reddy \*, N. V. 2004. Optimal part deposition orientation in FDM by using a multicriteria genetic algorithm. *International Journal of Production Research*, **42(19)**, 4069–4089.
- Popescu, D., Zapciu, A., Amza, C., Baci, F., & Marinescu, R. 2018. FDM process parameters influence over the mechanical properties of polymer specimens: A review. *Polymer Testing*, **69**, 157–166.
- Sachyani Keneth, E., Kamysny, A., Totaro, M., Beccai, L., & Magdassi, S. 2021. 3D Printing Materials for Soft Robotics. *Advanced Materials*, **33(19)**, 2003387.
- Tay, Y. W. D., Panda, B., Paul, S. C., Noor Mohamed, N. A., Tan, M. J., & Leong, K. F. 2017. 3D printing trends in building and construction industry: a review. *Virtual and Physical Prototyping*, **12(3)**, 261–276.
- Thrimurthulu, K., Pandey, P. M., & Venkata Reddy, N. (2004). Optimum part deposition orientation in fused deposition modeling. *International Journal of Machine Tools and Manufacture*, **44(6)**, 585–594.
- Yavuz, İ., Erçek, E., & Yuran, A. F. 2021. Ulaştırma Sektöründe İmdat Çekici Tasarımı ve 3B Yazıcı ile Üretimi. In *International Journal of Multidisciplinary Studies and Innovative Technologies*, **5 (1)**, 46–49.
- Yilmaz, C., Akalin, C., Kocaman, E. S., Suleman, A., & Yildiz, M. (2016). Monitoring Poisson's ratio of glass fiber reinforced composites as damage index using biaxial Fiber Bragg Grating sensors. *Polymer Testing*, **53**, 98–107.
- Zaldivar, R. J., Witkin, D. B., McLouth, T., Patel, D. N., Schmitt, K., & Nokes, J. P. (2017). Influence of processing and orientation print effects on the mechanical and thermal behavior of 3D-Printed ULTEM® 9085 Material. *Additive Manufacturing*, **13**, 71–80.